FLAx-REinforced Aluminum (FLARE)

A Bio-Based Fiber Metal Laminate Alternative Combining Impact Resistance and Vibration Damping

Alcaraz, Mathilde ; Alderliesten, René C.; Mosleh, Yasmine

Important note
To cite this publication, please use the final published version (if applicable).
Please check the document version above.

FLAx-REinforced Aluminum (FLARE): A Bio-Based Fiber Metal Laminate Alternative Combining Impact Resistance and Vibration Damping

Mathilde Alcaraz, René C. Alderliesten,* and Yasmine Mosleh

Fiber metal laminates (FMLs) have mainly been used in aerospace applications with synthetic fibers. To improve their environmental credentials and address issues regarding the end-of-life of these materials, a shift to FMLs based on natural fibers can be a promising course of action. However, regarding them as conventional FMLs overlook some of the unique benefits of natural fibers. Therefore, this study pioneers the examination of FLAx-REinforced aluminum (FLARE) for its combined impact resistance and vibration damping. Dynamic mechanical analysis and vibration beam tests demonstrate that the metallic layer predominantly influences the damping behavior of FLARE. The loss factor notably decreases with aluminum addition (by 80% compared to the flax composite), approximated via an inverse mixture rule. Low-velocity impact tests highlight the role of aluminum layers in energy absorption and the composite strength as a critical factor in impact resistance. FLARE exhibits 25% less specific energy absorption compared to its glass fiber counterpart. A quasi-static analytical model suggests the potential of FLARE for practical applications. With its balance of properties and considering its potential advantages at end-of-life, allowing recycling of aluminum, and its expected lower carbon footprint, FLARE renders potential beyond the aerospace sector, e.g., in other forms of transportation.

M. Alcaraz, R. C. Alderliesten
Aerospace Structures and Materials
Faculty of Aerospace Engineering
Delft University of Technology
Kluyverweg 1, 2629 HS Delft, The Netherlands
E-mail: r.c.alderliesten@tudelft.nl

Y. Mosleh
Biobased Structure and Materials
Faculty of Civil Engineering and Geosciences
Delft University of Technology
Stevinweg 1, 2628 CN Delft, The Netherlands

The ORCID identification number(s) for the author(s) of this article can be found under https://doi.org/10.1002/adem.202400183.

1. Introduction

Fiber metal laminates (FMLs) have been developed to create a material with inherent resistance to crack growth, combining thin metallic layers with a fiber-reinforced composite for excellent fatigue and corrosion resistance, and good mechanical properties while maintaining lightweight characteristics. GLAss-REinforced aluminum (GLARE), notably used in the Airbus A380's upper fuselage, is a well-known example.[1] However, the application of the FML concept is primarily limited to aerospace, relying heavily on synthetic fibers with notable environmental impacts. Indeed, the use of synthetic fibers enhances the FML-specific properties, but their environmental drawbacks, including energy-intensive production and difficulty in recycling, pose significant challenges. Therefore, with growing concerns about climate change, there is a need to explore a new generation of FMLs with lower embodied energy to reduce the carbon footprint of final products and more energy-efficient end-of-life scenarios. GLARE indeed presents challenges in component separation at the end of its life cycle. While the polymer can be incinerated with energy recovery, separating the glass fibers from the molten aluminum remains a hurdle. In contrast, FLAx-REinforced aluminum (FLARE) offers a more straightforward approach. Its aluminum layers can be recycled directly by concurrently incinerating the flax fibers and polymer matrix, with the potential for energy recovery during the incineration process.

Currently, efforts focus on developing bio-based composites, with natural fibers gaining importance for their low density, promising mechanical properties, and cost-effectiveness.[2,3] Among them, flax fiber composites exhibit excellent specific tensile and bending stiffness, making them suitable for transport and construction applications.[4] Additionally, they possess good thermal insulation properties and exhibit excellent damping capabilities compared to conventional composites due to their multiscale and hierarchical structure, which facilitates multiscale friction mechanisms.[5–7] However, their use is often limited to nonstructural parts due to inherent limitations such as low strength, high moisture absorption, poor thermal stability, and flammability concerns.[6,8] Moreover, flax fiber composites fracture at a considerably lower impact force compared to the force necessary to induce fiber breakage in their glass fiber counterparts.[9,10]

**ADVANCED
SCIENCE NEWS**

www.advancedsciencenews.com

**ADVANCED
ENGINEERING
MATERIALS**

www.aem-journal.com

Nevertheless, they absorb more energy during impact. Notably, studies by Wambua et al. reveal that among natural fibers, flax fibers excel in energy absorption during ballistic impact due to their higher strain to failure.[11] Furthermore, flax fibers offer environmental advantages over synthetic fibers including lower embodied energy, being less toxic for workers, and contributing negatively to global warming due to their carbon capture during plant growth. Additionally, the production process for flax fibers is less energy-intensive and less harmful to the environment compared to glass fibers.[12]

Therefore, combining flax fiber-reinforced epoxy (FFRE) with metal layers could leverage a synergistic effect, extending their use in FMLs to structural components and areas that have not been previously explored. Unfortunately, there is limited research on the mechanical properties of natural fiber-based FMLs, especially flax fiber metal laminates. Indeed, given the properties of flax fibers, it would probably not be viable to replace the commercialized GLARE, which is made from S2-glass fibers, with FLARE, particularly for strength-based designs. Hence, current literature primarily focuses on fiber hybridization, replacing a portion of synthetic fibers with natural fiber. These FMLs, combining synthetic fibers with natural fibers like flax, sugar palm, jute, or kenaf fibers, aim to mitigate environmental impact and costs while maintaining mechanical properties akin to conventional FMLs.[13–15] However, the challenge of recyclability persists as only some fibers are biodegradable, driving further investigation into natural fiber-based FMLs. Despite encouraging findings, natural fiber FMLs encounter obstacles such as low fiber strength, inconsistent properties, and inadequate fiber-matrix adhesion.[13,16] Nevertheless, recent advancements in fiber manufacturing processes and fiber-matrix adhesion techniques offer avenues for improvement. Moreover, they are most often envisaged for very demanding aeronautical applications and studied as a replacement for GLARE through conventional tensile, compression, or fatigue testing methodologies. However, the use of the FML concept can be seen in a different light and goes beyond aeronautical applications: enabling the use of flax fiber-based composites, for applications in which vibration damping should be minimized, and combined with improving their impact resistance through the use of metal layers. Indeed, the literature highlights that the application of a metal sheet bonded to the surface of a flax fiber composite improves its impact resistance, similar to the FML concept while increasing energy absorption compared with a monolithic metal.[11,17] Addressing this gap in the literature could provide valuable insights into the performance of metal laminates based on flax fibers for applications requiring both impact resistance and vibration absorption, capitalizing on the merits of flax fiber metal laminates, beyond their lower environmental footprint (due to the lower embodied energy of flax fibers, and the possibility of recycling aluminum with energy recovery).

In the end, the fundamental question revolves around whether the use of the FML concept with bio-based composites results in a synergistic material property apart from favorable environmental benefits. This study aimed to investigate and characterize the properties of FLARE, focusing specifically on its key distinguishing features, namely, its vibration damping and impact resistance capabilities which were not previously scrutinized. The damping characteristics of FLARE were analyzed and juxtaposed with those of FFRE and E-GLAss-REinforced aluminum (E-GLARE). The aim was to determine whether FLARE retains the advantageous vibration-damping properties inherent to flax fiber composites. This evaluation considered the influence of both the metal volume fraction (MVF) and the fiber orientation. Concurrently, the low-velocity impact resistance of FLARE was compared with that of E-GLARE, with a focus on assessing the influence of MVF and fiber type. Lastly, the study delved into the examination of analytical tools capable of predicting FML properties, such as the MVF method, specifically in the context of FLARE, and either validated existing tools or identified new ones as needed. This study does not delve further into other significant properties like durability, with for example hygrothermal aging, or fatigue, as they are already extensively documented and comprehended for FMLs and flax fiber composites.[8,16,18,19]

2. Methodology

2.1. Materials

A range of FMLs and composites were manufactured using unidirectional dry fabrics impregnated by hand with the RESOLTECH 1200/1204 epoxy system.[20] For the flax fiber reinforced panels, the ampliTex UD 280gsm fabric from Bcomp was used, while the E-glass fiber reinforced panels were produced using a quasi-unidirectional fabric from Saertex (U-E-640gsm).[21,22] In the cases of FLARE and E-GLARE, the core material was sandwiched between two pretreated sheets of 2024-T3 aluminum, with a thickness ranging from 0.3 to 0.5 mm.[23] Similar to the aluminum employed in producing GLARE for the A380, these sheets underwent chromic acid anodization and are coated with BR 127 primer. This process enables the creation of a protective layer to prevent corrosion and improves adhesion with the epoxy resin.[24]

2.2. Manufacturing Method

Considering the use of dry fabrics, the conventional autoclave process used for FMLs is not suitable. Therefore, a wet-layup process, in conjunction with vacuum bagging, has been adopted for both FML and composite panel production.

The materials forming the layup were cut to the appropriate dimensions. To enhance the adhesion of the composite core with the pretreated aluminum sheets, the latter underwent a degreasing process using a 2-butanone solution and was lightly abraded with Scotch Brite (3M). Following this, a secondary cleaning step with the 2-butanone solution was performed to eliminate residual dust and organic dirt and to activate the primer in preparation for the layup.

The layup process starts with the placement of the bottom aluminum layer on a flat mold that had been treated with a release agent. The metallic sheet is coated with a thin layer of premixed and degassed epoxy. Subsequently, plies of dry flax or E-glass fabric are manually laid on top and impregnated with epoxy resin to form a $[0°/90°]_s$ composite. This procedure is repeated until the top metal layer is positioned. In the case of composite panels, a similar approach is adopted, but the layup is constructed between two flat mold plates to ensure consistent manufacturing conditions. To complete the process, a vacuum bag is applied on top.

This serves several functions, including the application of consolidation pressure, elimination of entrapped air and volatile compounds during the curing process, and removal of excess resin that has been absorbed by the flax fibers. Instead of aiming for a full vacuum, which could lead to excessive resin extraction, a moderately high vacuum level was employed (60% of full vacuum). This compromise effectively facilitated the removal of air bubbles and allowed for a satisfactory degree of laminate compaction. Finally, the plates are cured at room temperature for 24 h under 400 mbar, followed by an oven postcure for 16 h at 60 °C, thereby ensuring the production of a high-quality laminate.

The cross-ply FFRE plate, with a fiber volume fraction of 43%, featured a nominal thickness of 1.86 ± 0.03 mm and a density of 1.21 ± 0.02 g cm^{-3}. In parallel, the cross-ply E-glass fiber-reinforced epoxy composite (E-GFRE), having a fiber volume fraction of 52.4%, displayed a nominal thickness of 1.92 ± 0.03 mm and a density of 1.81 ± 0.02 g cm^{-3}. Their respective void contents were assessed by microscopy, yielding values of 6.76% for FFRE and 7.99% for E-GFRE. The FML plates exhibited a 2/1 lay-up configuration, consisting of a $[0°/90°]_s$ fiber-reinforced polymer laminate layer. Their properties are given in **Table 1**.

The GLARE sample exhibits a higher fiber volume fraction compared to the FLARE sample due to flax fibers absorbing a considerable amount of resin during the impregnation process, limiting the fiber content. Moreover, the void content values obtained are relatively high compared to those achievable through manufacturing techniques utilizing prepregs and show a deviation that indicates the repeatability limits of the manual impregnation process. Nevertheless, the impact of these defects on mechanical performance is mitigated in the context of fiber–metal laminates.[25]

The composite and FML plates were finally cut into coupons, using water jet cutting and the shear guillotine, respectively, for the tests described in the following sections.

2.3. Experimental Methods

2.3.1. Low-Velocity Impact on FMLs

A series of single low-velocity impact tests were carried out at room temperature on rectangular samples of FMLs (150×100 mm^2). The test methodology and parameters were derived from Morinière's work on low-velocity impact on FMLs.[26,27] The tests were conducted using an in-house instrumented drop-weight tower equipped with a semihemispherical indenter nose, depicted in **Figure 1**. The impactor, with a total mass of 1.70 kg, impacted the sample at its center. A load cell

positioned on top of the indenter was responsible for measuring the contact force $F(t)$, while the impactor's velocity, both before and after impact, was measured using a high-speed camera.

For each sample type, an up-and-down approach, as described in ASTM D5420 standard,[28] was employed to determine the energy required to fully perforate the sample but not penetrate it, which is indicated by the presence of a visible crack along the diameter of the contact area on the aluminum rear side. The rectangular specimens are clamped using two frames with an aperture of 125 by 75 mm, as depicted in Figure 1. They are fastened in place by applying a torque of 40 Nm on each bolt to ensure good clamping during testing.

The force signal was integrated numerically to derive the velocity $V(t)$, displacement $d(t)$, and absorbed energy $E(t)$. The measured data were filtered to remove noise and a moving average was applied to minimize scatter in the force data and highlight significant variations.

2.3.2. Dynamic Mechanical Analysis (DMA)

DMA was carried out on both the FML and composite rectangular samples, following ASTM D5023-15 standard using the RSA-G2 Solid Analyzer by TA Instruments.[29] This method involves applying oscillatory deformation to the sample while tracking its response across different time (time sweep), temperature (temperature sweep), or frequency ranges (frequency sweep). By comparing stress and strain responses, the materials' viscoelastic behavior can be characterized. This study specifically focused on energy dissipation under cyclic loading, measured by the tangent of the phase shift between stress and strain ($\tan(\delta)$), which directly reflects the damping properties of the material. For testing, a three-point bending configuration was used as it offers the ideal mode of deformation for measuring medium to high-modulus materials. Moreover, this setup minimizes clamping effects that can impact damping behavior. To ensure consistent deformation while adhering to the force limit of the machine, the dimensions of each rectangular sample were adjusted with a width varying between 10 and 11.5 mm, and a span length of 25 or 40 mm.

To measure the loss factor ξ at a specific frequency for both FML and composite samples, oscillatory time sweeps were conducted at room temperature with a frequency of 1 Hz and a strain amplitude of 0.01%. This strain amplitude was chosen to ensure the samples remained within the linear viscoelastic region, as determined through dynamic strain sweeps. Various configurations were tested to assess the influence of metallic layer thickness and volume fraction, as well as fiber orientation within the

Table 1. Manufacturing properties of the different FMLs manufactured.

	Thickness [mm]	Fiber volume fraction [%]	MVF [%]	Void content [%]	Density [g cm^{-3}]
FLARE 5–2/1–0.5[a]	2.89 ± 0.04	42.1	34.6	13.5	1.72 ± 0.01
FLARE 5–2/1–0.4	2.67 ± 0.07	42.9	30.0	15.3	1.63 ± 0.09
FLARE 5–2/1–0.3	2.54 ± 0.01	41.2	23.6	5.89	1.57 ± 0.01
GLARE 5–2/1–0.3	2.61 ± 0.08	50.1	23.0	13.1	1.94 ± 0.02

[a]Sample naming follows the convention established by Roebroeks.[24]

**ADVANCED
SCIENCE NEWS**

www.advancedsciencenews.com

**ADVANCED
ENGINEERING
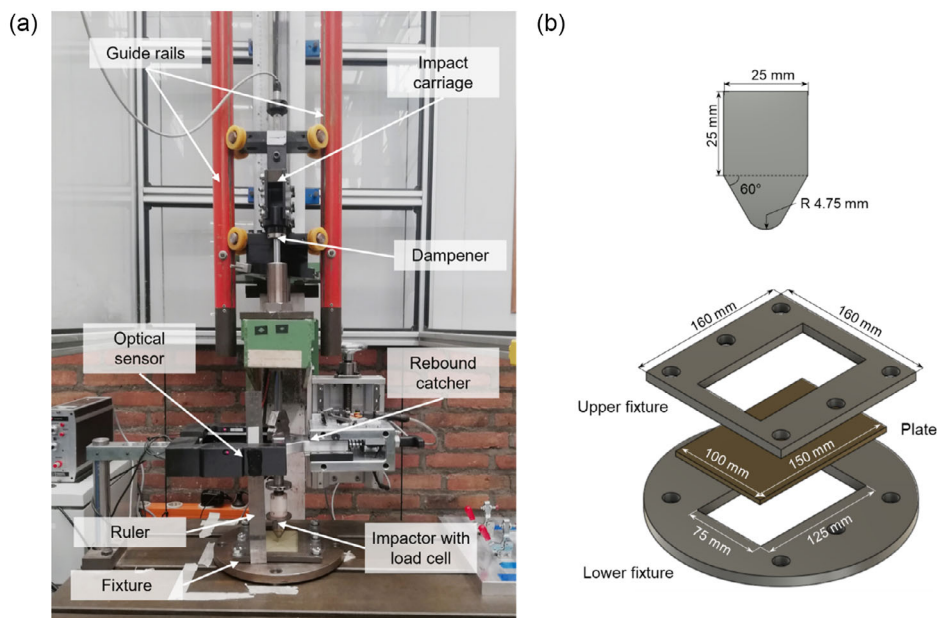MATERIALS**

www.aem-journal.com

Figure 1. a) In-house instrumented drop-weight tower. b) Impactor nose and fixture geometry.

composite layer. Particular attention was given to the symmetrical cross-ply configuration for FML, as it is considered a promising choice for achieving impact resistance and vibration damping, as suggested by the literature.[24]

2.3.3. Vibration Beam Test

Another way to assess the structural damping is to perform vibration beam tests, following the ASTM 5756-05 standard.[30] The experimental configuration centers around a cantilever beam, which is set into free vibration through the application of an excitation signal via one transducer, while another transducer captures the response of the beam. In this specific investigation, the excitation force was generated using an automatic impulse hammer vImpact-61 by Maul–Theet, chosen for its consistency in producing input signals, which in turn enhances measurement repeatability. For response measurement, a noncontacting transducer, the PSV-500 laser scanning vibrometer by Polytec,

was used to ensure precision and minimize additional damping during data collection. **Figure 2** illustrates the experimental setup, positioned on an optical table for isolation from external vibrations.

The dimensions of the rectangular samples were adapted to match their eigenfrequencies and provide a meaningful comparison of the damping for the different eigenmodes. Using the Euler–Bernoulli beam theory, the free length of the samples ranged from 170 mm for the most flexible samples to 250 mm for the stiffest ones, with a consistent width of 20 mm.

The frequency response function was evaluated, as an average over ten consecutive measurements, at multiple measurement points to reconstruct the deflection profile of the beam. Finally, a modal analysis was performed to extract a set of vibration modes and their associated modal parameters, among which the loss factor was calculated using the half-power bandwidth method.[31] This process allows for more accurate and reliable characterization of the structural dynamic behavior.
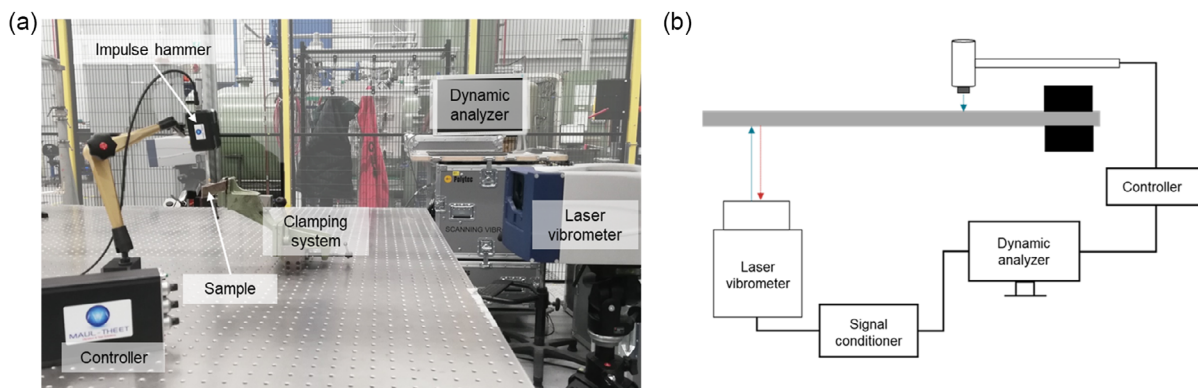

Figure 2. a) Vibration beam test setup on an optical table. b) Schematic diagram of the experimental setup.

3. Analysis and Prediction of Low-Velocity Impact

3.1. General Approach

To predict the low-velocity impact behavior of an FML, theoretical models have been developed using a quasi-static approach and mass-spring-damper systems to model the dynamics of the impact.[32–34] However, these approaches primarily consider energy dissipation due to plate deformation, overlooking critical factors like delamination, which also play a significant role in the impact process.[26] That is why an energy balance framework associated with plate theory has been chosen in this study.

The model introduced in this research is an extension of Morinière's work, aiming to predict the perforation behavior of FMLs subjected to low-velocity impacts and to offer a failure sequence to evaluate the contribution of individual components to the energy absorption process.[26]

The stresses induced by the deformation of the plate are calculated with the classical laminate theory (CLT) until failure is detected, using the material properties given in **Table 2** for the aluminum and **Table 3** for the composites.

A notable disparity exists between the coefficients of thermal expansion of the metal layers and those of the composite. This mismatch results in residual stresses within the laminate, with tensile stresses occurring in the metal layers and compressive stresses in the fiber layers. Although these stresses are low, given

Table 2. Aluminum alloy 2024-T3 properties.[23,27]

	Symbol [unit]	Aluminum alloy 2024-T3
Density at 23 °C	ρ [g cm^{-3}]	2.78
Tensile Young's modulus	E [GPa]	71.5
Yield tensile strength	σ^{yield} [MPa]	351
Ultimate tensile strength	σ^{ult} [MPa]	480
Poisson ratio	μ [–]	0.33
Coefficient of thermal expansion	α [°C^{-1}]	23.4×10^{-6}

Table 3. FFRE and E-GFRE properties.

	Symbol [unit]	FFRE[a]	E-GFRE[b]
Density at 23 °C	ρ [g cm^{-3}]	1.2	1.86
Longitudinal tensile modulus	E_1 [GPa]	28.9	37.9
Transversal tensile modulus	E_2 [GPa]	2.88	8.5
Ultimate longitudinal strength	σ_1^{ult} [MPa]	301	1080
Ultimate transversal strength	σ_2^{ult} [MPa]	14.6	39
Ultimate shear strength	τ_{12}^{ult} [MPa]	26.5	89
Poisson ratio	μ	0.42	0.33
Longitudinal coefficient of thermal expansion	α [°C^{-1}]	0.63×10^{-6c}	6.10×10^{-6}
Transversal coefficient of thermal expansion	α [°C^{-1}]	76.5×10^{-6c}	26.2×10^{-6}

[a]Results obtained for a fiber volume fraction of 45%. [b]Values adapted from the material data by Isaac et al.[44] for a fiber volume fraction of 50%. [c]Calculated using the relationships given by Schapery and the fiber and matrix properties.[45]

the low temperatures applied during the manufacturing process (only 60 °C during postcuring stage), they are taken into account in the model by adding them to the stresses calculated with the CLT.

Given the materials' sensitivity to strain rate, the model incorporates the influence of strain rate, which can be estimated, in the case of low-velocity impact, by dividing the impact velocity by half of the average plate dimensions. Notably, higher strain rates result in an increase in both the tensile strengths of composites and the yield strength of aluminum. Specifically, a strain rate of 100 s^{-1} leads to a 10% strength increase in glass fiber composite,[27] while a strain rate of 80 s^{-1} results in an $\approx$17% increase in flax fiber composite strength.[35] Finally, the yield strength of thin aluminum sheets increases to 375 MPa at a strain rate of 100 s^{-1}.[26]

3.2. Plate Deformation Profile

The plate deformation profile under low-velocity impact, derived from plate theory, is determined from the contact between the impactor and plate which leads to a bidirectional deflection profile of the neutral line of the FML plate. The contact radius is assumed to be equal to the tangency radius throughout the impact.

This profile must conform to the boundary conditions of a plate that is completely clamped and is specifically designed for an impact occurring at the exact center of the plate. Furthermore, in the current scenario, we anticipate a significant deflection of the plate, which allows us to disregard in-plane deformations in the formulation. By assuming that the flexural profile of an FML is a combination of the metallic layers and the composite layers, we can derive the deflection profile of the neutral axis of the laminate based on the work of Morinière et al. as expressed by Equation (1):[27]

$$w(x, y) = \begin{cases} (1) & \Delta \\ (2) & \text{MVF} \cdot w_{0_{AL}} \left(1 - \dfrac{x}{\alpha a}\right)^m \left(1 - \dfrac{y}{\beta b}\right)^m + \dots \\ & \dots (1 - \text{MVF}) \cdot w_{0_{GE}} \left[1 - \left(\dfrac{x}{\alpha a}\right)^n\right] \left[1 - \left(\dfrac{y}{\beta b}\right)^n\right] \end{cases}$$

(1)

(1) $0 \leq x \leq R_a \ 0 \leq y \leq R_b$;
(2) $R_a \leq x \leq \alpha a \ R_b \leq y \leq \beta b$.

where Δ is the maximum displacement at the plate center, a is the plate length, and b is its width.

3.3. Stress Analysis: CLT

Using the derived deflection profile, the Von Kármán strains, which characterize the substantial deflection of thin plates, are determined by adhering to the Kirchhoff hypothesis for displacement fields. Subsequently, the CLT is employed to compute the stresses in each layer of the laminate and perform the failure analysis. Additionally, the initial curing stresses arising from the manufacturing process are incorporated into the analysis.

The failure assessment in the model relies on the Von Mises criterion for metallic layers and the Tsai–Hill criterion for composite layers. When a layer experiences failure, its elastic properties are promptly degraded, and the stresses of the failed layer

are redistributed among the unaffected layers based on their respective stiffness properties.

To account for the strain-hardening behavior of the metal layers, modifications are introduced to the CLT, as outlined by Alderliesten.[18] The Ramberg–Osgood relationship is employed to calculate a virtual modulus of plasticity used in the CLT framework when the aluminum yield strength is exceeded. Notably, in contrast to prior studies, a minimum threshold of 650 MPa is established for the virtual modulus, consistent with the tangent of the second portion of the stress–strain curve for aluminum.[36]

3.4. Energy Calculation and Impact Response

Energy analysis is conducted to ascertain the impact response of the FML. The process involves integrating the strain energy throughout the thickness of the laminate, which can be subdivided into three components: membrane energy (U_m), bending energy (U_b), and the energy arising from membrane-bending coupling (U_c). The values for these components are determined by leveraging the ABD matrix associated with the laminate.[37] For a quarter of the plate:[26]

$$
\begin{aligned}
U_m = \int_{R_a}^{\alpha a} \int_{R_b}^{\alpha b} & \left\{ \frac{1}{8} A_{11} \left(\frac{\partial w}{\partial x}\right)^4 + \frac{1}{4} A_{12} \left(\frac{\partial w}{\partial x}\right)^2 \left(\frac{\partial w}{\partial \gamma}\right)^2 \right. \\
& + \frac{1}{8} A_{22} \left(\frac{\partial w}{\partial \gamma}\right)^4 + \frac{1}{2} \left[A_{16} \left(\frac{\partial w}{\partial x}\right)^2 + A_{26} \left(\frac{\partial w}{\partial \gamma}\right)^2 \right] \frac{\partial w}{\partial x} \frac{\partial w}{\partial \gamma} \\
& \left. + \frac{1}{2} A_{66} \left(\frac{\partial w}{\partial x} \frac{\partial w}{\partial \gamma}\right)^2 \right\} dx d\gamma = w_0^4 K_m
\end{aligned}
$$

$$
\begin{aligned}
U_c = - \int_{R_a}^{\alpha a} \int_{R_b}^{\beta b} & \left\{ \frac{1}{4} B_{11} \left(\frac{\partial w}{\partial x}\right)^2 \frac{\partial^2 w}{\partial x^2} + \frac{1}{2} B_{12} \left[\left(\frac{\partial w}{\partial \gamma}\right)^2 \frac{\partial^2 w}{\partial x^2} \right. \right. \\
& \left. + \left(\frac{\partial w}{\partial x}\right)^2 \frac{\partial^2 w}{\partial \gamma^2} \right] + \frac{1}{4} B_{22} \left(\frac{\partial w}{\partial \gamma}\right)^2 \frac{\partial^2 w}{\partial \gamma^2} \\
& + B_{16} \left[\frac{\partial^2 w}{\partial x^2} \frac{\partial w}{\partial x} \frac{\partial w}{\partial \gamma} + \left(\frac{\partial w}{\partial x}\right)^2 \frac{\partial^2 w}{\partial x \partial \gamma} \right] \\
& + B_{26} \left[\frac{\partial^2 w}{\partial \gamma^2} \frac{\partial w}{\partial x} \frac{\partial w}{\partial \gamma} + \left(\frac{\partial w}{\partial \gamma}\right)^2 \frac{\partial^2 w}{\partial x \partial \gamma} \right] \\
& \left. + 2 B_{66} \frac{\partial^2 w}{\partial x \partial \gamma} \frac{\partial w}{\partial x} \frac{\partial w}{\partial \gamma} \right\} dx d\gamma = w_0^3 K_c
\end{aligned}
$$

$$
\begin{aligned}
U_b = \int_{R_a}^{\alpha a} \int_{R_b}^{\beta b} & \left[\frac{1}{2} D_{11} \left(\frac{\partial^2 w}{\partial x^2}\right)^2 + D_{12} \frac{\partial^2 w}{\partial x^2} \frac{\partial^2 w}{\partial \gamma^2} + \frac{1}{2} D_{22} \left(\frac{\partial^2 w}{\partial \gamma^2}\right)^2 \right. \\
& + 2 \left(D_{16} \frac{\partial^2 w}{\partial x^2} + D_{26} \frac{\partial^2 w}{\partial \gamma^2} \right) \frac{\partial^2 w}{\partial x \partial \gamma} \\
& \left. + 2 D_{66} \left(\frac{\partial^2 w}{\partial x \partial \gamma}\right)^2 \right] dx d\gamma = w_0^2 K_b
\end{aligned}
$$

$$(2)$$

Besides accounting for strain energy, the energy dissipated due to delamination is also taken into consideration. Assuming a simplified concentrated force scenario, the advancement of a single mode II central delamination occurs when the force resulting from plate deformation exceeds a critical threshold force.[27] The expression for this threshold force (F_{del}) is given by Equation (3):

$$
F_{del} = \sqrt{\frac{8\pi^2 E_{lam} t_{lam}^3 G_{IIc}}{9(1 - \nu_{lam}^2)}}
\tag{3}
$$

where, E_{lam}, t_{lam}, and ν_{lam} correspond to the plate's stiffness, thickness, and Poisson's ratio, respectively. A mode II interlaminar fracture toughness value of $0.44\,\text{N mm}^{-1}$ is applied for E-GFRE and FFRE composites.[9,38] Subsequently, the associated delamination energy is computed as:

$$
E_{del} = \frac{2\pi E_{lam} t_{lam}^2 G_{IIc}^2}{9(1 - \nu_{lam}^2) \tau_{12}^{ult}}
\tag{4}
$$

Ultimately, the total energy absorbed during the impact encompasses both the energy dissipated in each occurrence via plate deformation and delamination. From this, the impact velocity can be determined by considering kinetic energy, and the reduction in velocity during the impact response curves can be expressed as:

$$
\frac{1}{2} m V_{i+1}^2 = \frac{1}{2} m V_i^2 - E_{abs_i}
\tag{5}
$$

4. Results and Discussion

4.1. Low-Velocity Impact Behavior of FLARE

Figure 3 depicts the force–displacement curves of FLARE 5–2/1 samples with different aluminum thicknesses and GLARE 5–2/1–0.3. In the case of FLARE, the graphs reveal the presence of multiple force peaks which can be a characteristic feature of the impact response of structures with complex deformation behavior. The first peak can be associated with energy absorption through delamination or other failure mechanisms within the composite ply, while the second peak corresponds to primary aluminum layer failure. As the MVF increases, the prominence of the first force peak diminishes, likely due to the influence of the metallic layers.

A comparison of impact responses for various FLARE samples indicates that increasing aluminum layer thickness affects the impact behavior, as anticipated the impact energy required to cause full perforation increases with the MVF. This observation might suggest that the impact behavior of FLARE is dominated by aluminum. However, as the thickness of the aluminum layer increases, so does the overall thickness of the laminate. And this increase in thickness has a significant effect on the impact behavior of FLARE. The type of fiber also plays a crucial role in impact behavior. In fact, the maximum impact force of GLARE 5–2/1–0.3 is comparable to that of FLARE with thicker aluminum layers. Finally, increasing the MVF results in greater specific energy absorption, with FLARE 5–2/1–0.5 absorbing 30% more energy by unit of weight than FLARE 5–2/1–0.3, and FLARE absorbing 25% less energy by unit of weight than GLARE with the same aluminum thickness.

Regarding impact-induced damage, characteristic patterns are observed on both the front and back aluminum layers, as shown in **Figure 4**, resembling those seen in GLARE samples by Morinière.[26] The front aluminum layer exhibits a crack along
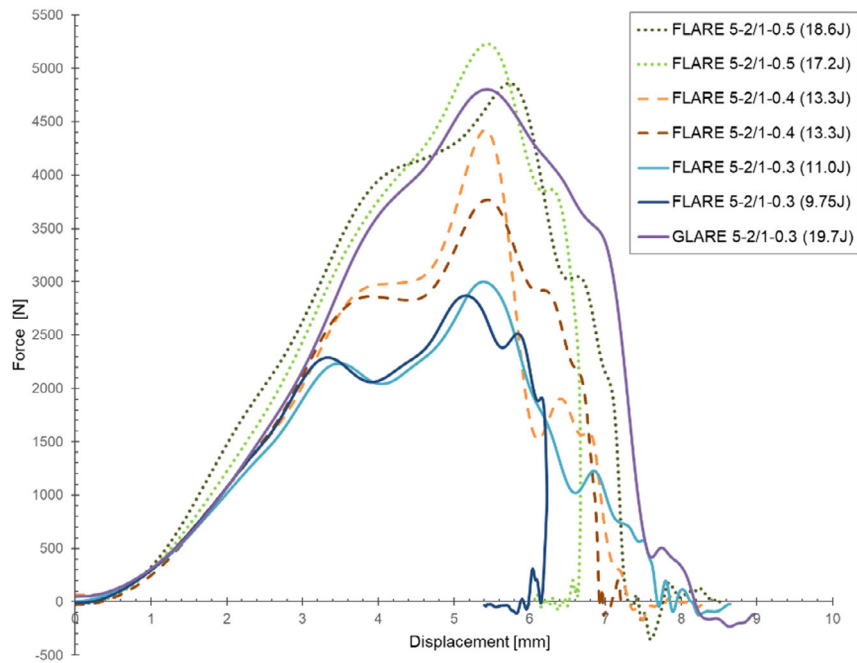
ADVANCED
SCIENCE NEWS

www.advancedsciencenews.com

ADVANCED
ENGINEERING
MATERIALS

www.aem-journal.com

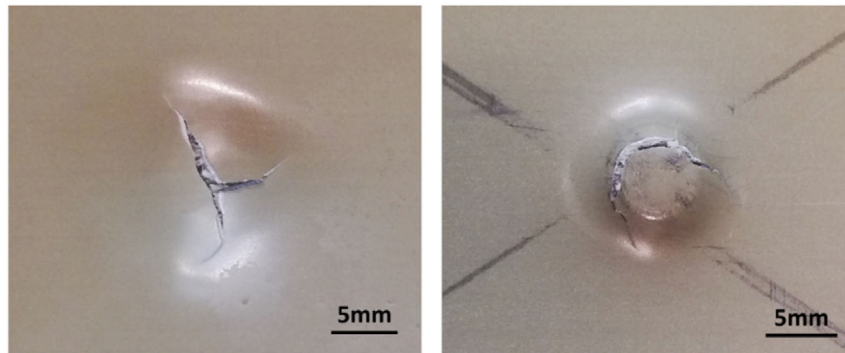**Figure 3.** Force–displacement curves of FLARE 5–2/1 and GLARE 5–2/1–0.3 samples.

Figure 4. Impact damage in FLARE 5–2/1–0.5 for the rear side (left) and front side (right).

the periphery of the impact site, while the back aluminum layer displays a crack extending across the diameter of the impacted region. To be more specific, two distinct types of damage were observed on the rear side. The damage either manifests as a crack running perpendicular to the outer fiber direction (for FLARE 5–2/1–0.5 and some of FLARE 5–2/1–0.4) or as a crack following the rolling direction of the aluminum layer (observed in FLARE 5–2/1–0.4 and FLARE 5–2/1–0.3), which is parallel to the outer fiber direction. According to Vlot, they are respectively indicative of impact behavior dominated by fibers or aluminum.[32] This implies that, depending on the thickness of the aluminum layer, both failure modes can occur. A parallel observation was noted in GLARE, which exhibits diverse failure modes based on the behavior of glass fibers and the layup of the laminate.[32,33]

Additionally, a comparison with the prediction using the analytical model was performed. The prediction generally aligns with test results but often overestimates the maximum force,

underestimates absorbed energy, and impacts velocity. Apart from the aforementioned overestimations and underestimations, the force–displacement model curves, as shown in **Figure 5**, exhibit a pronounced initial force peak, which corresponds to the failure of the first composite ply for the FLARE samples. In the analytical model, the failure criteria assume the rupture of an entire ply, an occurrence unlikely to happen. Likewise, the proposition that a failed layer at the impact site will no longer support load corresponds to an unrealistic situation. These assumptions could account for the presence of the peak load that is not captured during testing.[26]

Moreover, in the model, the final layer failure occurs at the same force as the preceding failure event, attributed to a catastrophic failure. Additionally, the laminate's spring back is accounted for in the model, whereas it does not appear to be captured by the test results. Finally, predicted energy–displacement curves, depicted in Figure 5, show a substantial underestimation
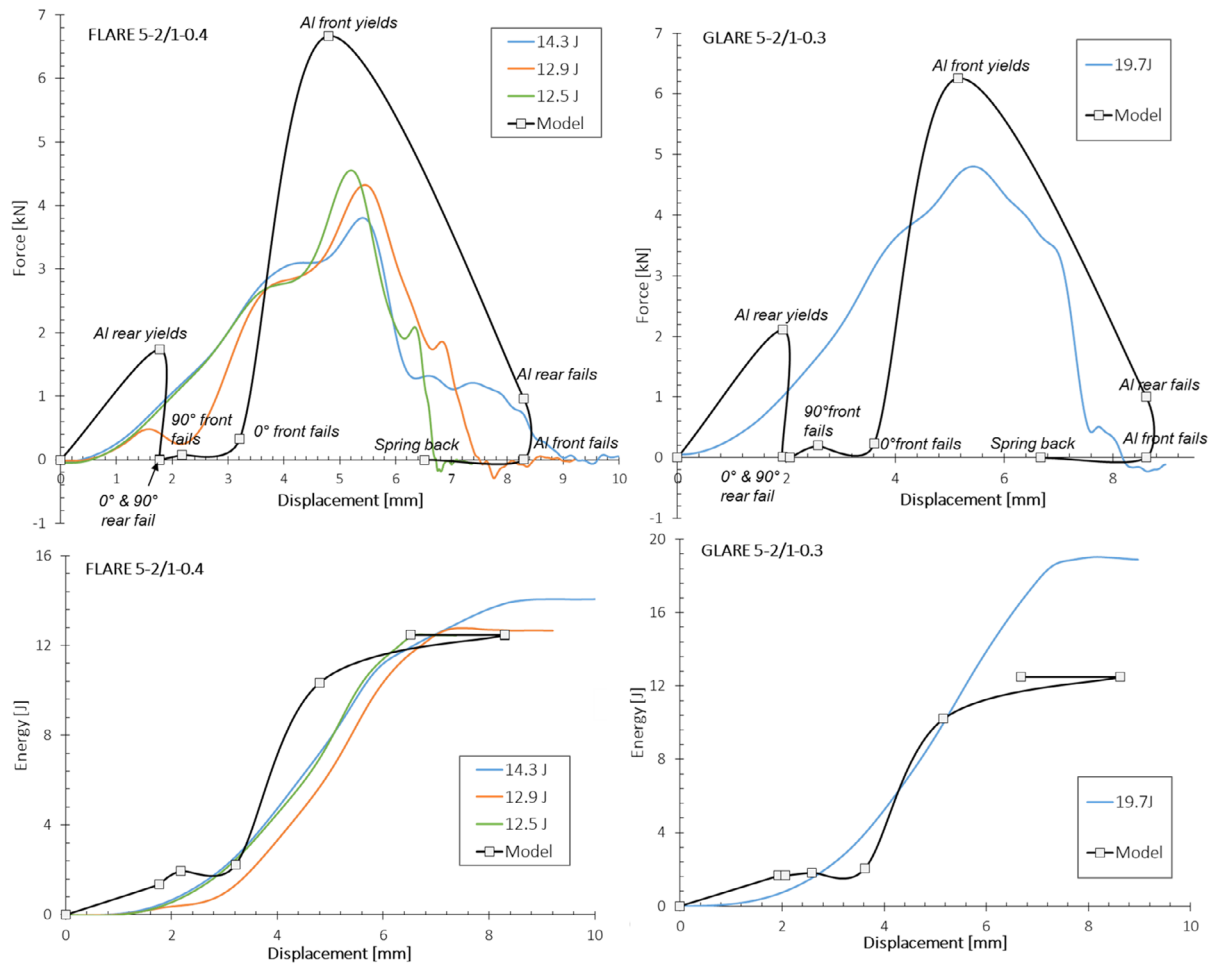
**ADVANCED
SCIENCE NEWS**

www.advancedsciencenews.com

**ADVANCED
ENGINEERING
MATERIALS**

www.aem-journal.com

Figure 5. Comparison between analytical model and experimental results for the impact response of FLARE 5–2/1–0.4 and GLARE 5–2/1–0.3.

of absorbed energy. This could be due to an underestimation of the absorbed energy associated with delamination and/or the omission of the energy dissipated by other failure modes such as fiber breakage and petaling in the energy calculation. The unsatisfactory outcomes highlight the model's limitations when applied to current, thicker FMLs, necessitating adjustments in deformation theory and failure criteria. Particularly, the transverse shear deformations can no longer be neglected. Thus, the utilization of First- or Higher-order Shear Deformation Theory becomes essential for the computation of stresses, and the failure criteria must be adapted.

4.2. Vibration Damping

4.2.1. DMA Results

Figure 6 presents a bar chart illustrating outcomes of loss factor measured by DMA for different fiber orientations, types, and the presence or not of a metallic layer. As expected, FFRE demonstrates superior damping compared to its glass fiber counterpart, particularly in the [0°/90°]$_s$ layup, boasting a damping coefficient twice as high on average. However, the distinction diminishes
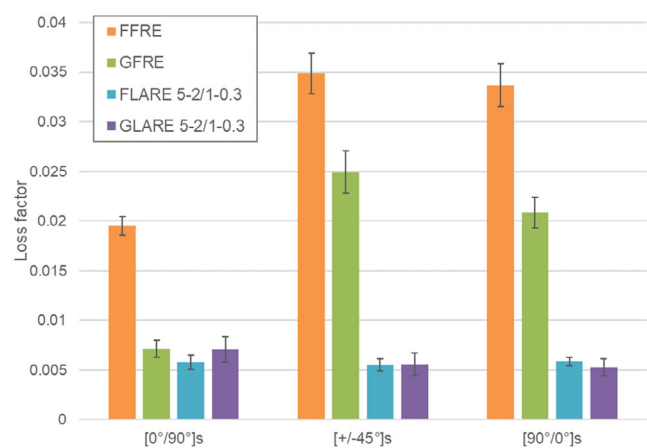

Figure 6. Comparison of the loss factor for different fiber orientations for the composite and FML samples.

when examining FLARE and GLARE samples, as they exhibit nearly identical loss factors. Notably, FFRE shows a significant 80% decrease in the loss factor compared to FLARE, with

FLARE even surpassing GFRE in certain layup cases like [90°/0°]ₛ and [±45°]ₛ.

In terms of the influence of fiber orientation, it appears that the [±45°]ₛ configuration showcases the most effective damping behavior in the composite samples. However, the fiber orientation has no discernible effect on the FML samples. This can be explained by the significantly higher stiffness of the metal component compared to the composite, which takes precedence in overall deformation and limits the involvement of other layers in absorbing vibrations. This implies that the damping characteristics of an FML are likely primarily influenced by the metal component rather than the composite itself. Fiber type and orientation appear to play a less significant role in shaping the damping behavior of FML.

Following that, the experimental results for each configuration are compared to predictions made using various types of rules of mixture (or MVF), which incorporate either volume fractions or weight fractions. The comparisons for the [0°/90°]ₛ configuration are illustrated in **Figure 7**. For aluminum, the loss factor is derived from the damping coefficient of 0.0012 provided in the literature.[39]

Upon examination of the graphs, it becomes evident that the straightforward MVF method or rule of mixture (ROM) falls short in providing a satisfactory approximation of the loss factor. In fact, it predicts values on average two and a half times higher than the experimental values, a discrepancy reduced to twice as much when considering weight fractions. Additionally, the rule of mixture based on an energy approach (EROM), occasionally referenced in the literature,[40–42] was also compared to the experimental results. It is expressed by:

$$\xi_{FML} = MVF \frac{E_{Al}}{E_{FML}} \xi_{Al} + (1 - MVF) \frac{E_{FFRE}}{E_{FML}} \xi_{FFRE} \quad (6)$$

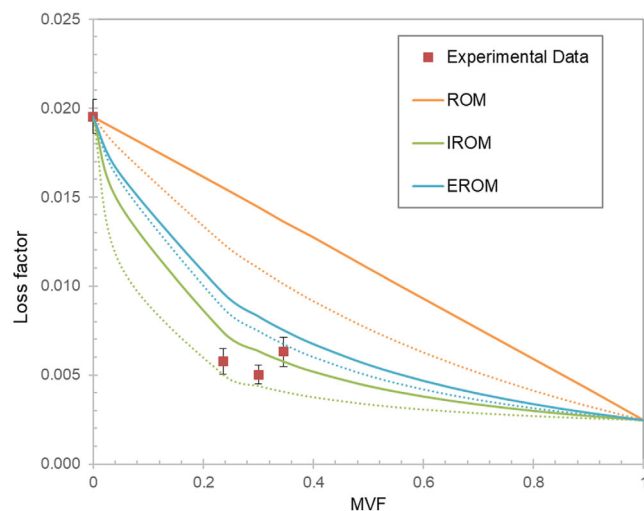where E represents Young's modulus of the material and ξ its loss factor.

Figure 7. Comparison between the experimental loss factor measured by DMA (symbols) and predicted loss factor using different rules of mixture with volume fractions (solid lines) or weight fractions (dashed lines), for the [0°/90°]ₛ configuration.

However, it is the inverse rule of mixture (IROM), specifically the one utilizing the weight fraction of metal, which proves to be the most accurate for all the configurations tested. Its equation, employing the weight fraction of metal (MWF), is:

$$\frac{1}{\xi_{FML}} = \frac{MWF}{\xi_{Al}} + \frac{(1 - MVF)}{\xi_{FFRE}} \quad (7)$$

The IROM, employed for loading perpendicular to the stacking sequence direction, operates similarly to an electrical circuit in series. In this analogy, the laminate can be conceptualized as a series of mass-spring-damper systems arranged sequentially to mitigate vibrations. Hence, it is fitting to use this approach to predict the damping coefficient of such a hybrid material. Using the weight fraction instead of the volume fraction provides a better fi, highlighting the mass of the system and accentuating the contribution of the dominant metal in the damping behavior. However, the prediction tends to underestimate the loss factor. By calculating the average relative deviation between the first two experimental data points and the curve in Figure 6, an underestimate of ≈12% is derived. Notably, this method overlooks the energy that could be dissipated at the interface between the composite and metallic layers, potentially explaining the disparity between theory and experiment. This estimation excludes the third data point due to its discrepancy, as explained in the subsequent discussion.

Another notable observation from the graph is that the loss factor of FLARE 5–2/1–0.5 samples surpasses that of FLARE 5–2/1–0.3 samples. This difference can be explained by the relatively small sample size, which results in highly localized measurements. Consequently, it is possible that singularities, such as voids, are more prevalent in the FLARE 5–2/1–0.5 samples, despite multiple tests being conducted. Moreover, the discrepancy is further supported by **Figure 8**, illustrating that the FML plates, from which the samples were extracted, do not have the same void distribution. The high void content is associated with pore connectivity, which causes a discontinuity in the fiber/matrix interface. This significant discontinuity leads to inadequate adhesion between the reinforcement and the matrix, resulting in increased energy dissipation through friction and consequently a higher loss factor.

Thus, it is recognized that the experimental data should also account for the void content, and it is anticipated that the outcomes obtained in this study might exhibit an overestimation when compared with those of a theoretical void-free sample. This consideration is not limited to the present results but may also extend to earlier findings in the literature where DMA results are presented without specifying the porosity content.[5,43] Finally, more experiments are needed to quantify the porosity's influence on the loss factor. Nonetheless, this does not alter the primary conclusions drawn regarding FML design, indicating that metal predominantly governs vibration-damping behavior.

4.2.2. VBT Results

Figure 9a illustrates the influence of fiber type on the loss factor measured by vibration beam test in two distinct configurations. As expected, the FFRE sample displays significantly higher damping capabilities, with a loss factor 2–3 times greater than
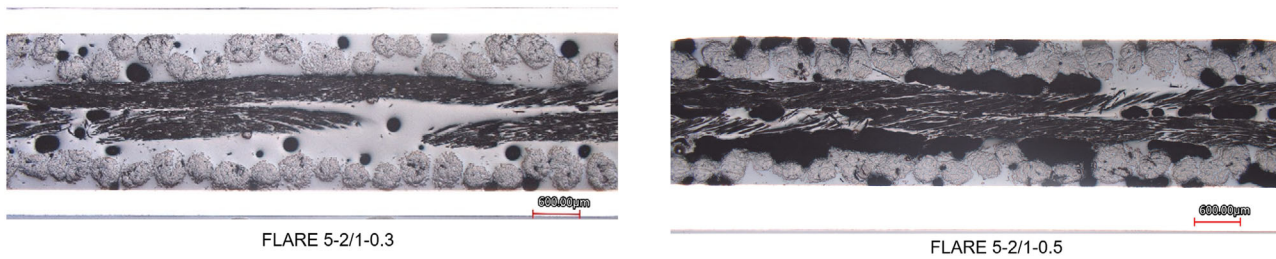
FLARE 5-2/1-0.3   FLARE 5-2/1-0.5

Figure 8. Micrographs of FLARE 5–2/1–0.3 and FLARE 5–2/1–0.5 sheets, illustrating the difference in porosity content and distribution.
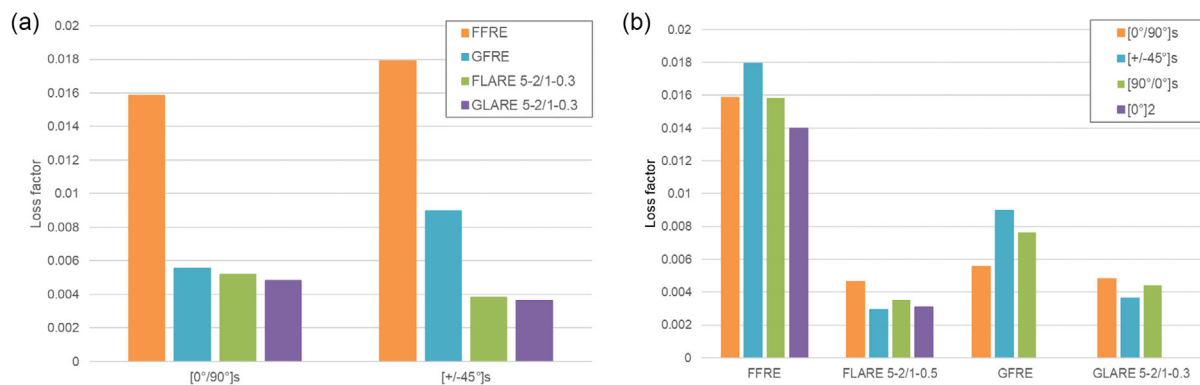

Figure 9. a) Comparison of the loss factor for different fiber orientations for the composite and FML samples with a comparable MVF. b) Influence of fiber orientation on the loss factor for the different samples. All the values correspond to the first bending mode of each sample.

its glass fiber counterpart. However, the introduction of 3 mm thick aluminum layers eliminates this difference, indicating that in the case of FMLs, the damping behavior is dominated by the metal component, as observed with DMA results.

For the impact of fiber orientation, Figure 9b provides a clearer perspective for both composite and FML samples. Again, the $[\pm45°]_s$ configuration exhibits the highest damping performance for both FFRE and GFRE, while the unidirectional orientation shows the lowest damping. Specifically, there is a relative difference of 28% between the two configurations for FFRE. This can be attributed to the in-plane shear strain energy of composites, reaching its peak for this specific fiber orientation. However, for FLARE and GLARE, the correlation between the loss factor and fiber angle seems less obvious or even nonexistent. Like DMA, this could be attributed to a relatively smaller change in stiffness due to the presence of aluminum layers, reinforcing the conclusion that the damping behavior is primarily influenced by the metal components.

As for DMA, a comparison between experimental data and predictions based on different rules of mixture is performed. **Figure 10** showcases the results for the 1st bending mode of the $[0°/90°]_s$ configuration. In line with DMA, the same three predictive rules are presented in the context of vibration beam test (VBT), utilizing either the MVF or metal weight fractions, considering a damping coefficient of 0.0012 for aluminum.

Consistently, the IROM using the metal weight fraction provides the most accurate approximation, slightly overestimating the results with an average relative difference of 17%. The convex
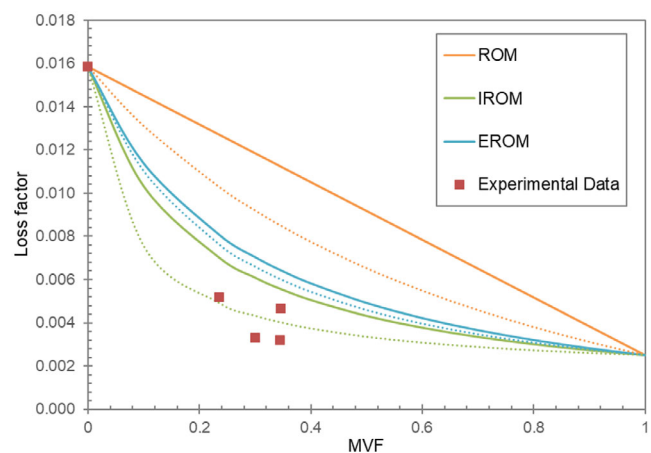

Figure 10. Comparison between the experimental loss factor measured via VBT (symbols) and predicted loss factor using different rules of mixture with volume fractions (solid lines) or weight fractions (dashed lines), for the $[0°/90°]_s$ configuration in 1st bending mode.

curvature of the predictive curve distinctly reflects the dominance of aluminum in the vibration-damping behavior.

In the case of FLARE 5–2/1–0.5, specimens from two different plates were tested, and the data from each plate are presented separately. A notable discrepancy of 31% between these two data points is observed. As with the DMA results, this difference can

be attributed to a different porosity distribution between the two plates. Consequently, it is probable that the samples exhibiting the higher loss factor contain a greater void content (13.5% void vs 10% void for the plate yielding lower loss factor samples). A higher void content is linked to lower stiffness, resulting in an improved ability to deform and, consequently, a higher capacity to dissipate energy. Additionally, voids introduce an additional source of internal friction, making them overall beneficial for damping. Similar conclusions are drawn for the second bending mode and the other configurations. However, when considering the 3rd mode of vibration, the combination of bending and torsion leads to an overestimation of the loss factor. Consequently, the predictions using the IROM appear to be less accurate (Figure S1, Supporting Information).

4.2.3. Comparison of DMA and VBT

Based on the damping results obtained through DMA and VBT, a comparative analysis between the two measurement methods is viable. Notably, the loss factors measured during the vibration beam test consistently appear lower than those obtained through DMA. This finding resonates with Duc et al.'s work,[5] where they explained this discrepancy by attributing it to the diverse energy dissipation modes occurring for small and larger deformations within the composite. Additionally, the difference in loss factors is more pronounced for the composite samples compared to FMLs. This corresponds to the notion that in FMLs, the damping behavior is primarily governed by the metal layer, making it less susceptible to changes in dissipative friction mechanisms. The vibration frequency also plays a role, allowing more time for the sample to dissipate energy at low frequency.

It is also crucial to acknowledge the inherent differences in the test setups, particularly in terms of boundary conditions. The clamping of the beam in VBT may introduce an additional source of damping compared to DMA, which is considered clamp-free. Nevertheless, given that both tests are conducted at relatively low frequencies and small amplitudes, any additional damping resulting from air friction can be disregarded and treated as negligible.

5. Summary and Conclusion

The primary goal of this study was to experimentally investigate the impact and damping characteristics of FLARE, addressing a gap in prior research. Furthermore, this study aimed to validate and potentially modify existing predictive analytical models tailored to conventional fiber metal laminates to ensure their applicability to FLARE, with flax fibers possessing a bilinear stiffness behavior.

It was observed that FLARE's vibration damping is predominantly governed by its metal component, with the loss factor decreasing as MVF increases. Low-velocity impact tests revealed similarities with conventional FMLs like GLARE, albeit with lower impact resistance in FLARE. Nonetheless, this discrepancy is mitigated when considering the energy absorbed per unit weight. Composite layers in FLARE played a minor role in energy absorption, while metal layers deformed significantly before failure, emphasizing their key role. Various predictive tools were

scrutinized, with the IROMs and quasi-static analytical model showing promise for approximating FLARE behavior in vibration damping and low-velocity impact, respectively.

The study underscores the potential of FLARE to enhance the use of bio-based materials in structural applications, offering good mechanical properties as a result of the FML concept. Combining flax fiber composites with metal results in a material with a specific stiffness comparable to E-GLARE and superior to E-glass fiber composites (see Figure S2, Supporting Information for modulus calculation via the MVF method). Thus, for applications relying on stiffness-based designs, FLARE emerges as a more environmentally friendly alternative to both E-GLARE and GFRE, addressing recycling challenges effectively.

Finally, delving into the potential of this synergistic hybridization from a novel perspective of combining impact resistance with vibration absorption creates opportunities for identifying applications where FLARE emerges as a compelling choice. Notably, in the realm of transportation, FLARE proves to be a promising choice, such as lightweight and rigid structures for shipping container panels that demand weather resistance. Additionally, in situations like wind turbine blades, necessitating a favorable stiffness-to-weight ratio and GFRE presents challenges in recycling, FLARE emerges as a compelling and promising solution.

Supporting Information

Supporting Information is available from the Wiley Online Library or from the author.

Conflict of Interest

The authors declare no conflict of interest.

Data Availability Statement

The data that support the findings of this study are available from the corresponding author upon reasonable request.

**ADVANCED
SCIENCE NEWS**

www.advancedsciencenews.com

**ADVANCED
ENGINEERING
MATERIALS**

www.aem-journal.com

[1] E. C. Botelho, R. A. Silva, L. C. Pardini, M. C. Rezende, *Mater. Res.* **2006**, *9*, 247.

[2] Z. Zhang, S. Cai, Y. Li, Z. Wang, Y. Long, T. Yu, Y. Shen, *Compos. Sci. Technol.* **2020**, *194*, 108151.

[3] D. U. Shah, *J. Mater. Sci.* **2013**, *48*, 6083.

[4] T. H. Panzera, T. Jeannin, X. Gabrion, V. Placet, C. Remillat, I. Farrow, F. Scarpa, *Composites, Part B* **2020**, *197*, 108049.

[5] E. Duc, P.-E. Bourban, J.-A. E. Månson, presented at *Eur. Conf. Compos. Mater.*, Seville, Spain, **2014**.

[6] L. Yan, N. Chouw, K. Jayaraman, *Composites, Part B* **2014**, *56*, 296.

[7] M. Rueppel, J. Rion, C. Dransfeld, C. Fischer, K. Masanie, *Compos. Sci. Technol.* **2017**, *146*, 1.

[8] S. Liang, P. Gning, L. Guillaumat, *Compos. Sci. Technol.* **2012**, *72*, 344.

[9] R. Panciroli, B. O. Giannini, *Compos. Struct.* **2021**, *264*, 113750.

[10] F. Bensadoun, D. Depuydt, J. Baets, I. Verpoest, A. W. van Vuure, *Compos. Struct.* **2017**, *176*, 933.

[11] P. Wambua, B. Vangrimde, S. Lomov, I. Verpoest, *Compos. Struct.* **2007**, *77*, 232.

[12] A. L. Duigou, P. Davies, C. Baley, *J. Biobased Mater. Bioenergy* **2011**, *5*, 153.

[13] M. Chandrasekar, M. R. Ishak, M. S. Salit, Z. Leman, M. Jawaid, J. Naveen, *BioResources* **2018**, *13*, 5725.

[14] N. L. Feng, S. D. Malingam, K. A. Zakaria, M. Z. Selamat, *J. Sandwich Struct. Mater.* **2019**, *21*, 2440.

[15] M. A. A. El-Baky, A. E. Alshorbagy, A. M. Alsaeedy, M. Megahed, *J. Nat. Fibers* **2022**, *19*, 303.

[16] E. Kandare, S. Yoo, V. Chevali, A. Khatibi, *Fatigue Fract. Eng. Mater. Struct.* **2018**, *41*, 1691.

[17] K. R. Ramakrishnan, M. Kanerva, E. Sarlin, M. Hokka, *Int. J. Lightweight Mater. Manuf.* **2022**, *5*, 29.

[18] R. C. Alderliesten, in *Fatigue and Fracture of Fibre Metal Laminates*, Springer, Delft, The Netherlands **2017**.

[19] J. Rousseau, N. E. N. Donkeng, F. Farcas, S. Chevalier, V. Placet, *Composites, Part A* **2023**, *171*, 107582.

[20] Resoltech, https://www.resoltech.com/en/markets/1200-detail.html (accessed: November 2023).

[21] Bcomp, https://www.bcomp.ch/products/amplitex/, (accessed: November 2023).

[22] Saertex, https://www.saertex.com/en/products/datasheet-glass, (accessed: November 2023).

[23] T. J. D. Vries, PhD Thesis, Delft University of Technology, **2001**.

[24] G. H. J. J. Roebroeks, in *Fiber Metal Laminates* (Eds: A. Vlot, J.W. Gunnink), Springer, Dordrecht, Netherlands **2001**.

[25] E. Kroon, G. Roebroeks, J. W. Gunnink, Influence of general quality on Glare material performance, Tech. Rep. TD-R-02-007 FMLC, Delft, The Netherlands **2002**.

[26] F. D. Morinière, PhD Thesis, Delft University of Technology, **2014**.

[27] F. D. Morinière, R. C. Alderliesten, R. Benedictus, *Mech. Mater.* **2013**, *66*, 59.

[28] ASTM D5420, ASTM International, PA 19428-2959, United States, **2004**.

[29] ASTM D5023, ASTM International, PA 19428-2959, United States, **2015**.

[30] ASTM E756, ASTM International, PA 19428-2959, United States, **2017**.

[31] Half bandwidth, ASTM International, PA 19428-2959, United States, **2017**.

[32] M. Sadighi, R. C. Alderliesten, R. Benedictus, *Int. J. Impact Eng.* **2012**, *49*, 77.

[33] A. Vlot, *Compos. Eng.* **2012**, *3*, 911.

[34] F. D. Morinière, R. C. Alderliesten, R. Benedictus, *Int. J. Impact Eng.* **2014**, *67*, 27.

[35] W. Wang, X. Zhang, N. Chouw, Z. Li, Y. Shi, *Compos. Struct.* **2018**, *200*, 135.

[36] P. Soltani, M. Keikhosravy, R. H. Oskouei, C. Soutis, *Appl. Compos. Mater.* **2011**, *18*, 271.

[37] C. Kassapoglou, in *Design and Analysis of Composite Structures*, John Wiley & Son Ltd, Chichester, West Sussex, United Kingdom **2010**.

[38] Y. Saadati, J. F. Chatelain, G. Lebrun, Y. Beauchamp, P. Bocher, N. Vanderesse, *J. Compos. Sci.* **2020**, *4*, 66.

[39] E. C. Botelho, L. C. Pardini, M. C. Rezende, *Mater. Sci. Eng. A* **2005**, *399*, 190.

[40] J. M. Berthelot, Y. Sefrani, *Compos. Struct.* **2007**, *79*, 423.

[41] M. J. L. Guen, R. H. Newman, A. Fernyhough, G. W. Emms, M. P. Staiger, *Composites, Part B* **2016**, *89*, 27.

[42] J. Vantomme, *Composites* **1995**, *26*, 147.

[43] E. Sarlin, Y. Liu, M. Vippola, M. Zogg, P. Ermanni, J. Vuorinen, T. Lepistö, *Compos. Struct.* **2012**, *94*, 3327.

[44] D. M. Isaac, I. Ori, in *Engineering Mechanics of Composite Materials*, Oxford University Press, New York **2006**.

[45] R. A. Schapery, *J. Compos. Mater.* **1968**, *2*, 380.